Bioactive Materials 35 (2024) 122–134

Contents lists available at ScienceDirect

Bioactive Materials

journal homepage: www.keaipublishing.com/en/journals/bioactive-materials

Silk fibroin-based inks for *in situ* 3D printing using a double crosslinking process

Francesca Agostinacchio [a,b], Vincent Fitzpatrick [d], Sandra Dirè [c], David L. Kaplan [d], Antonella Motta [b,*]

[a] National Interuniversity Consortium of Material Science and Technology, Florence, Italy
[b] BIOtech Research Center and European Institute of Excellence on Tissue Engineering and Regenerative Medicine, Department of Industrial Engineering, University of Trento, Trento, Italy
[c] Materials Chemistry Group & "Klaus Müller" Magnetic Resonance Laboratory, Department of Industrial Engineering, University of Trento, Trento, Italy
[d] Department of Biomedical Engineering, Tufts University, Medford, MA, 02155, USA

ARTICLE INFO

Keywords:
Silk fibroin inks
In situ 3D printing
Covalent crosslinking
Regenerative medicine
Rapid gelation

ABSTRACT

The shortage of tissues and organs for transplantation is an urgent clinical concern. *In situ* 3D printing is an advanced 3D printing technique aimed at printing the new tissue or organ directly in the patient. The ink for this process is central to the outcomes, and must meet specific requirements such as rapid gelation, shape integrity, stability over time, and adhesion to surrounding healthy tissues. Among natural materials, silk fibroin exhibits fascinating properties that have made it widely studied in tissue engineering and regenerative medicine. However, further improvements in silk fibroin inks are needed to match the requirements for *in situ* 3D printing. In the present study, silk fibroin-based inks were developed for *in situ* applications by exploiting covalent crosslinking process consisting of a pre-photo-crosslinking prior to printing and *in situ* enzymatic crosslinking. Two different silk fibroin molecular weights were characterized and the synergistic effect of the covalent bonds with shear forces enhanced the shift in silk secondary structure toward β-sheets, thus, rapid stabilization. These hydrogels exhibited good mechanical properties, stability over time, and resistance to enzymatic degradation over 14 days, with no significant changes over time in their secondary structure and swelling behavior. Additionally, adhesion to tissues *in vitro* was demonstrated.

1. Introduction

The shortage of tissues/organs transplantation remains a global challenge, with only 10% of needs being met [1]. To potentially fill some of this gap, 3D (bio)printing is a technology that can offer a solution. 3D printing enables reproducible, standardized, and personalized manufacturing of 3D architectures to mimic native tissue and organ structures [2,3]. Numerous 3D printing techniques have been developed including extrusion-based, and light-based techniques such as digital light processing, stereolithography, volumetric 3D printing [4–6]. However, there are intrinsic limitations in the application of *in vitro* 3D printing to optimize clinical translation, including mismatches between the fabricated implant and the expected/unexpected defect size *in vivo*, limitations with the biological evaluation performed *in vitro*, infection risks due to manipulation to transfer the implant in the surgical setting and during implantation, as well as integration of the printed materials with the native healthy tissue at the implant site *in vivo* [7,8]. Thus, more advanced options are needed, and *in situ* 3D printing as a personalized medicine approach is an evolving strategy. Here, 3D models can be elaborated starting from the patients' specific defect size and shape via images, to guide direct printing of the new tissue in the patient in the operating room, with anatomical accuracy and fidelity using minimally invasive routes [9,10]. By printing directly in the patient, there is the control in real time of the defect size, by inducing crosslinking of the ink *in situ*, and the body can then work as natural bioreactor [11]. In this scenario, two main approaches have been developed to achieve success [12,13]. The first one is based on a portable device, such as the Biopen [14,15], and the second, robotic arms to print with high precision along three axes via a surgeon-controlled console chi è sangue [16]. Both approaches exhibit some limitations, for the handled one, shape fidelity

Peer review under responsibility of KeAi Communications Co., Ltd.
* Corresponding author.
E-mail address: antonella.motta@unitn.it (A. Motta).

https://doi.org/10.1016/j.bioactmat.2024.01.015
Received 27 October 2023; Received in revised form 16 January 2024; Accepted 16 January 2024
2452-199X/© 2024 The Authors. Publishing services by Elsevier B.V. on behalf of KeAi Communications Co. Ltd. This is an open access article under the CC BY-NC-ND license (http://creativecommons.org/licenses/by-nc-nd/4.0/).

is dependent on surgeon skills and only superficial tissues such as skin can be reached, whereas in the robotic approach, the overall complexity of the procedure still hinders its application [17].

Ex situ and *in situ* 3D printing approaches applied to cartilage regeneration were compared [18]. Compared to canonical 3D *in vitro* printing techniques, there remain many issues with *in situ* applications. The *in situ* approach not only provides shape fidelity but offers more direct and rapid integration to the surrounding tissues, thereby avoiding complications with *in vitro* printed materials that require time to integrate and can lose interfaces with the surrounding tissues, resulting in complications in regeneration [17,18]. A key point in the development of *in situ* printing is the ink [19]. The ink must exhibit specific requirements including suitable rheological properties, adhesion to tissues, shape fidelity after deposition in the defect, and rapid gelation [9,20]. Moreover, compared to *in vitro* 3D printing, inks designed for *in situ* applications require a fixed printing bed temperature at 37 °C to simulate body temperature, whereas photo-crosslinking *in situ* may be problematic since irradiation in the body can be harmful [21] and light penetration into the depth of tissues is limited in order to reach internal organs [22].

Natural biopolymers are widely used for 3D printing [23,24]. Among these, silk fibroin, extracted from silkworm cocoons, has garnered significant scientific interest for biomedical applications in various material formats such as sponges, hydrogels, films, foams, aerosols, and fibers [25–31]. The interest in this protein polymer is due to its remarkable properties that make it an extremely versatile material [31]. Specifically, silk fibroin exhibits tunable mechanical properties and degradation rates, biocompatibility, aqueous processability, and self-assembly into β-sheets (crystallization). Some silk-based medical devices have been approved for use by the FDA [32]. Silk fibroin versatility can also be achieved by tuning molecular weight [33] and the amino acid sequences provide the basis for the unusual and important properties of this biomaterial. The silk protein is composed of a heavy (≈390 kDa) and light chain (≈26 kDa) [34], where the former is characterized by a hexapeptide repeated sequence which assembles into β-sheets, responsible for the slower degradation kinetics and higher mechanical strength [35]. Furthermore, the unique sequence of amino acids found in silk are provide sufficient chemically active amino acids (e.g., lysine, tyrosine, serine, glutamic acid, histidine, aspartic acid) for chemical modifications, to further help in tailoring the properties [36,37].

However, silk fibroin at relatively low concentrations exhibits low viscosity hindering application in extrusion-based 3D printing. To increase viscosity [38,39], high concentrations [40,41], blends with other biomaterials [39,42,43], crosslinking before printing [44], or printing in specific bath/sacrificial materials [40] are strategies that have been employed.

Several works report these aforementioned approaches to use silk fibroin in 3D printing applications [28,45,46]. For example, physical crosslinking was reported [41], mimicking silk assembly that takes place during silk spinning. High concentration (30 % w/V) of silk fibroin solution was used to print 3D architectures. The crosslinking was achieved by printing into an inorganic salt bath, which induced hydrogen bond formation, gelation, and increased β-sheet structure from 6% to 48%. The scaffolds generated exhibited shape fidelity and good mechanical strength [41]. Covalent crosslinking can be achieved via horseradish peroxidase (HRP) reactions to form dityrosine bonds [47]. Extrusion 3D printing of silk with HRP crosslinking has been reported for printing crypt-like structures for intestine tissue models, inducing gelation by fully crosslinking the ink before printing or by pre-crosslinking it before extrusion [44]. However, risks of nozzle clogging during the process remain a challenge. Dityrosine bond formation was also achieved via photo-crosslinking with riboflavin [48,49] or ruthenium [50] as photo-initiators, leading to more faster reactions compared to the enzymatic systems. Photo-crosslinking was also achieved via methacrylation of lysine residues, applied to digital light processing (DLP) reported for cartilage [45] and bone tissue [51] regeneration applications, where gelation is induced after printing.

However, to exploit the potential of pristine silk fibroin for *in situ* 3D printing it is necessary to avoid nozzle clogging when using high concentrations of the protein, overcome the low viscosity of silk solutions, and induce rapid crosslinking, among other challenges.

In this scenario, the aim of the present study was to design and develop silk-based inks for *in situ* applications through a reliable, and a versatile process, without any postprocessing manipulation and to overcome the various challenges highlighted above. A double crosslinking process was developed to address this goal, combining pregelation via incomplete photo-crosslinking followed by *in situ* HRP-driven gelation. The versatility of the process was demonstrated with two different silk molecular weights to show feasibility for *in situ* 3D printing. Additionally, the fundamental role of physical crosslinking induced by extrusion stress in the print nozzle was a focus towards rapid transition of random coils and β-turn structures to β-sheet formation, further stabilizing the gels over time. The printed hydrogels resulted in mechanically stable systems that supported bone marrow-derived human mesenchymal stem cell adhesion and viability, and good adhesion on mock tissues (e.g., raw chicken breast).

2. Materials and methods

2.1. Preparation of aqueous silk fibroin solutions

Silk fibroin was extracted and regenerated as described elsewhere [33,52]. Briefly, the degumming was performed by pouring 5 g of cut silk fibroin cocoons in 2 L of boiling water with 0.2 M of Na_2CO_3 (Merck Sigma Aldrich, Darmstadt, Germany). To obtain two different molecular weights of silk fibroin, the silk was boiled for 15 min (Silk 15 mB = minutes boiled) or 30 min (30 mB), equal to ca. 300 kDa and 200 kDa, respectively [53]. After boiling, silk was washed three times in DI water at room temperature for 20 min and later dried under a fume hood for 24 h. Dissolution was performed by dissolving the silk in 9.3 M aqueous solution of lithium bromide (LiBr, Merck Sigma Aldrich, Darmstadt, Germany) at a concentration of 20% (w/V). The solution was incubated for 2 h at 60 °C. Then, silk fibroin was chemically modified by performing a methacrylation reaction, as previously reported [54]. Specifically, glycidyl methacrylate (GMA - Merck Sigma Aldrich, Darmstadt, Germany) was added dropwise into the silk solution and reacted for 3 h under stirring at 60 °C [55]. This is a nucleophilic addition reaction, leading to the opening of the epoxy ring of the GMA that reacts with silk primary amines, forming di-β-hydroxyamide [54]. Fully dissolved, methacrylate silk (Sil-Ma) was later dialyzed against DI water for three days with regular water changes to remove LiBr and unreacted GMA. Finally, the solution was centrifuged twice for 20 min at 9000 rpm at 4 °C to remove impurities from the final solution. All the conditions were sterilized via filtration (Primo Vacuum Filter Systems, 0.45 μm, PES – Euroclone, Italy) [52,56]. The concentration was calculated from the dry weight. Unless otherwise stated, both Sil-Ma 15 mB and 30 mB were used at a concentration of 5% w/V.

2.2. UV spectroscopy – 2,4,6-trinitrobenzene sulfonic acid (TNBS) assay

TNBS assay was performed as previously reported [31,54] to measure the methacrylation degree on Sil-Ma solution. Briefly, since the GMA reacts with free amines along silk sequence, the quantification of free amine on methacrylate silk in comparison with unmodified silk was investigated. In detail, both unmodified silk (SF) and methacrylate silk (Sil-Ma) were diluted to a final concentration of 1 mg/mL. The test was carried out at pH 8.5, and for this reason, all the solution were dialyzed against $NaHCO_3$ to reach the desired pH. Calibration curve was prepared using as standard β-alanine (MW 89.09 Da) at known concentrations (see Table 1). After this, 300 μl of TNBS solution (Merck Sigma Aldrich, Darmstadt, Germany) at 0.02 (w/V) at pH 8.5 were added to 150 μl of all the standards and samples and incubated for 2 h at 40 °C ± 1 °C. After

Table 1
Calibration curve with known concentration of β-alanine.

Concentration mg/mL	Molarity M	Absorbance A
0.031	3.502×10^4	0.460
0.016	1.754×10^4	0.231
0.008	8.755×10^5	0.115
0.004	4.379×10^5	0.053
0.002	2.133×10^5	0.023
0	0	0

the incubation, the color of each sample shift to yellow-orange color according to free amine concentration. All the samples were transferred into a 96-well plate and absorbance was measured at 418 nm with a microplate reader (Tecan Infinite M200). Three replicates per condition were tested. The degree of substitution (DS) was calculated with the following formula: DS % = [1-(free amine concentration on Sil-Ma/free amine concentration on SF)]*100.

2.3. Sil-Ma hydrogels crosslinking process

Sil-Ma (5% w/V) was gently mixed with 0.02% (w/V) lithium phenyl-2,4,6-trimethylbenzoylphosphinate (LAP) (Merck Sigma Aldrich, Darmstadt, Germany) as photo-initiator, 0.01% (v/v) H_2O_2, and 10 U/mL of type VI horseradish peroxidase (HRP) (Merck Sigma Aldrich, Darmstadt, Germany). Next, the following steps were followed: (a) Pre-crosslinked gel formation: The solution was poured into a glass beaker and pre-photo-crosslinked by irradiation with a UV light source at 365 nm (I = 90 W/m^2) for 40 s (for Sil-Ma 30 mB, 60 s). This step led to the formation of a pre-photo-crosslinked gel, called PC (pre-crosslinked). Photo-crosslinking reaction is achieved thank to the formation of free radicals on silk fibroin chain after the activation of the LAP, under light exposure [54]. (b) Double crosslinked gel: after the pre-photo-crosslinking, HRP activation led to full gelation and this condition was named double crosslinked (DC). Samples without enzymatic crosslinking, but only subjected to the pre-photo-gelation (PC) process represented controls in the study.

2.4. Rheological analyses

All rheological analyses were performed with an HR2 Rheometer (TA Instruments, Delaware). Viscoelastic tests were carried out to verify the presence of a flow point in the different crosslinking phases, thus the printability of the materials, and to compare the behavior over time of PC and DC conditions. The flow point was verified by performing an oscillation amplitude test at constant frequency (1 Hz) and with increasing shear stress (up to 1000 Pa). The storage modulus G' over 24 h time frame was measured in the LVE region in oscillation time mode, at 1 Hz and 3 Pa for 3 min. As additional controls and to better characterize the materials, oscillation amplitude tests were performed on gels whose gelation was completed before printing, achieved via full photo-crosslinking (FC), and complete enzymatic crosslinking (EC) (Table 2).

After photo-crosslinking, the pre-gel was transferred into a 3D printing syringe (3 cc – Cellink, Sweden). 3D printing was performed with an extrusion 3D bioprinter, BioX (Cellink, Sweden). The printing head temperature was fixed at 20 °C to avoid premature activation of the HRP, thus leading to heterogeneous gelation. The printing bed temperature was 37 °C, to enhance optimal HRP activation conditions and to resemble physiological temperature. Sil-Ma-based inks were printed with a 22 G nozzle, at a print speed of 8–9 mm/s, and a pressure of 50–80 kPa. After extrusion, the printed structures were incubated at 37 °C for 1 h to complete the enzymatic crosslinking.

Table 2
List of tested conditions and description.

Conditions	Description
PC – Pre-Photo-Crosslinked	Pre-photo-crosslinking, incomplete
DC – Double Crosslinked	Pre-photo-crosslinking combined with enzymatic crosslinking (HRP-driven)
FC – Full Photo-Crosslinking	Full photo-crosslinking
EC – Full Enzymatic Crosslinking	Full complete, enzymatic crosslinking (HRP-driven)

2.5. Printability

Printability index (Pr) represents a key parameter to measure the accuracy of printed pores [39,57,58]. For this experiment, 20 mm grids were printed with two different grid infill, 10% and 15%. All the samples were printed with a 25G nozzle. After printing pictures were acquired and analyzed with ImageJ to measure the area and the perimeter of the squares inside each structure. After this, all the measures were averaged and printability index calculated according to the formula: $p^2/16A$, where p represents the perimeter of the pore and A the area. At least 3 replicates per condition were printed. High printing accuracy, thus high precision result in a Pr = 1, while values lower or higher indicate round and irregular geometries.

2.6. Infrared spectroscopy

Infrared spectroscopy was performed to evaluate the secondary structure of Sil-Ma inks before printing and the effect of shear stress in the nozzle on protein structure. Additionally, after printing both the PC and DC were incubated for 2 weeks in DI water and medium at 37 °C (DMEM high glucose – Euroclone, Italy) and the protein conformation over time was studied at days 1, 7, and 14, never drying the samples. Tests were performed with PerkinElmer Spectrum One Spectrophotometer (PerkinElmer, Waltham, MA, USA) in attenuated total reflectance (ATR-FTIR) mode. Prior to the test, to remove any interference of medium and water, all gels were washed three times in deuterated water (D_2O) (Merch Sigma Aldrich, Darmstadt, Germany). Spectra were acquired with 16 scans at 4 cm^{-1} resolution, in the wavenumber range of 550-4000- cm^{-1} to detect silk fibroin Amide I, II, and III at 1641, 1513, and 1233 cm^{-1}, respectively. To investigate silk secondary structure rearrangement, analysis of amide I peaks (1610-1705 cm^{-1}) was run with Fourier self-deconvolution following the protocol previously reported [31].

2.7. Swelling

Swelling behavior of DC and PC conditions was monitored over 14 days and studied at days 1, 7 and 14, in medium and DI water. Each sample was extruded for 20 s (ca. 200 μl of gel) into a silicone mold (n = 5) and the initial weight was measured (W_0). At each time point, the sample was blotted on paper to remove excess solvent and the final weight (W_1) was measured. The swelling percentage was calculated as (W_1/W_0) x 100. During the experiment, all the samples were incubated in an incubator at 37 °C.

2.8. Degradation

Samples were extruded as described in the previous paragraph and incubated in 2 mL of medium and water, and degradation was studied in the presence and absence of 0.001 U/mL Protease type XIV from *Streptomyces griseus* (Merck Sigma Aldrich Darmstadt, Germany). All the samples were incubated at 37 °C. Fresh enzyme was added every two days. At each time point (days 1, 7, and 14) medium or water was removed, the samples were washed overnight in ultrapure DI water, frozen at −80 °C, and then lyophilized. The dry weight was measured, and degradation reported as the residual mass percentage measured at

each time point compared to sample weight at time zero (t_0) (n = 4).

2.9. Mechanical compression

Unconfined compression was performed on DC and PC samples, incubated in both medium and DI water for 14 days. The test was carried out with a Bose Electroforce 3200 machine (TA Instruments, DE, USA) equipped with a 200 N load cell (sensitivity 0.05 N). A preload of 0.5 N and a compression rate of 0.5 mm/m were applied to all samples. The diameter and height of each sample was measured with a caliper prior to the test. The Young's modulus was calculated from the slope of the initial (linear) part of the curve.

2.10. Biological evaluation

For *in vitro* experiments, human bone marrow-derived mesenchymal stem cells (hBM-MSCs) from the American Type Culture Collection (ATCC) were used. The cells were cultured in expansion medium composed of DMEM High Glucose medium (Euroclone, Italy), supplemented with Fetal Bovine Serum (FBS, Euroclone, Italy) 15%, and antibiotic/antimycotic (Euroclone, Italy) 1%. The seeding density was $2*10^5$ cells/ml. Cells were cultured for 7 days and the medium was replaced every 3 days.

2.10.1. Confocal analysis

Confocal imaging (Nikon A1Laser Microscope – Japan) was performed to study cell adhesion. At each time point (days 1, 7), two replicates for each condition were analyzed. The samples were fixed with paraformaldehyde (PFA – Sigma Aldrich, Darmstadt, Germany) 4% and incubated at room temperature (RT) for 30 min. Subsequently, the samples were washed twice with PBS (Euroclone, Italy). Nuclei and cytoskeleton staining was performed by adding 4′,6-diamidino-2-phenylindole (DAPI – Sigma Aldrich, Darmstadt, Germany) and rhodamine phalloidin (Invitrogen - ThermoFisher – USA) according to the manufacturers' instructions, respectively. The samples were incubated at RT for 20 min, protected from light. Finally, two washes in PBS were performed and all the samples were observed by confocal microscopy.

2.10.2. AlamarBlue assay

Cell metabolism was measured by AlamarBlue assay. At each time point, four replicates for each condition and the blank controls (gels without cells) were incubated with resazurin reagent (Chemodex Ltd, Switzerland) 10% in complete medium at 37 °C for 3 h. Then 100 μL of the supernatant of each sample was transferred to a black 96-well plate in duplicate; the fluorescence intensity with excitation wavelength at 535 nm and emission at 590 nm were measured with a microplate reader (Tecan Infinite M200) using complete medium and the Alamar reagent as negative controls. Since the test was not disruptive, the sponges were later washed, new medium was added, and the plate was incubated at 37 °C until the next time point.

2.11. Statistical analyses

For AlamarBlue, GraphPad Prism 9.0 was used and samples in each condition were compared among the different time points with two-way Anova test and Tukey's multiple comparison test. Significance was attributed when $p < 0.05$ (*), $p < 0.01$ (**), $p < 0.001$ (***).

3. Results and discussion

3.1. Development of silk fibroin-based inks

For extrusion 3D printing techniques, the ink must exhibit shear thinning behavior, filament formation during extrusion, and a suitable viscosity (30 mPa*s to 6×10^7 mPa*s) [59,60]. Silk fibroin does not meet these parameters. Indeed, in Fig. S1, viscosity values of the Sil-Ma solution at the two molecular weights are reported, confirming what reported in literature [61]. Therefore, the first step in our design was to overcome the viscosity limitations. Two different silk molecular weights were selected, 15 mB and 30 mB, equal to ca. 300 kDa and 200 kDa, respectively [53]. To develop the ink, crosslinking processes leading to covalent bond formation were chosen to achieve more control over the structure, degradation kinetics, and mechanical properties. A double crosslinking process was designed, composed of a pre-gelation phase to make the silk fibroin extrudable, and an *in situ* second crosslinking to stabilize the printed structure (Fig. 1).

Since pre-gelation was achieved via photo-crosslinking, TNBS assay was performed to investigate if the methacrylation reaction with the GMA was successfully performed, thus, to quantify the degree of substitution (DS) of the methacrylate group on primary amines. The DS resulted to be equal to 67% ± 3%, confirming what previously reported in the literature [62]. After this, for pre-crosslinking, methacrylate silk fibroin (Sil-Ma) was photo-crosslinked leading to incomplete, covalently crosslinked gel formation (PC). The gelation was intentionally not completed to avoid the formation of fully-crosslinked gels which could otherwise clog during printing. This pre-crosslinking process was controllable, and the reaction activation was dependent on the time of light exposure time. In contrast, after printing, HRP-driven enzymatic crosslinking has been selected to stabilize and induce complete gelation at 37 °C by forming stable and covalent dityrosine bonds *in situ*. In details, phenols on tyrosine are oxidized when the HRP is in presence of the H_20_2. This reaction forms an intermediate compound with an oxyferryl center and a porphyrin-based cation radical. The now activated HRP undergoes two single electron oxidation reactions in the presence of tyrosine's phenol groups, generating phenol free radicals, thus forming dityrosine bonds [63,64]. Enzymatic crosslinking (EC) depends on many variables such as temperature, free radicals, silk concentration, peroxide concentration, as well as silk molecular weight [65], leading to heterogeneity when used as a pre-crosslinking process. Considering the silk fibroin amino acid composition, tyrosine represents ca. 5% of the total composition [66], and the formation of inter and intra-dityrosine bonds allows the formation of highly stable, elastic hydrogels [65].

To investigate if the double crosslinking (DC) approach was printable, and to verify if enzymatic crosslinking (EC) was leading to the complete gelation, rheological analyses were performed. For the assessment of printability, viscoelasticity studies were carried out with amplitude sweeps on the different compositions to investigate flow behavior. In particular, the flow point is the crossover point between the curves of loss and storage moduli (G″ and G′, respectively), corresponding to the conditions at which the material starts to flow. This is an important parameter for printability, specifically if shear can unfold and align the protein chains to allow flow through the nozzle [67]. However, high shear stresses might impact cell encapsulation in bioinks, or lead to irreversible ink deformation (e.g., in the case of silk crystallization) [68]. We compared the double crosslinking (DC) with the pre-photo-crosslinking condition (PC), adding as controls the fully photo-crosslinked gels (FC), and fully enzymatically crosslinked gels (EC). All the conditions exhibited viscoelastic behavior and had G′ higher than G''. In Fig. 2a, the 15 mB PC exhibited a flow point at a stress value of 82.3 Pa ±35.3 Pa. All other conditions, DC, FC, and EC did not show a flow point in the oscillation stress range analyzed. The behavior of the fully photo-crosslinked condition (FC) is shown as an example in Fig. 2b.

Although the flow point was not detected, the presence of a yield point identified the limit of the linear viscoelastic region. This also suggests that at higher stresses there may be a flow point. The same behavior was observed for fully enzymatic and double crosslinking conditions (Supplemental Data, Fig. S2a and b).

These results confirmed the initial hypothesis (Fig. 2a) that the 15 mB pre-crosslinking led to an extrudable, homogenous filament, whereas the other conditions resulted in clogging of the nozzle, heterogenous gelation (as for the EC), and higher extrusion pressures.

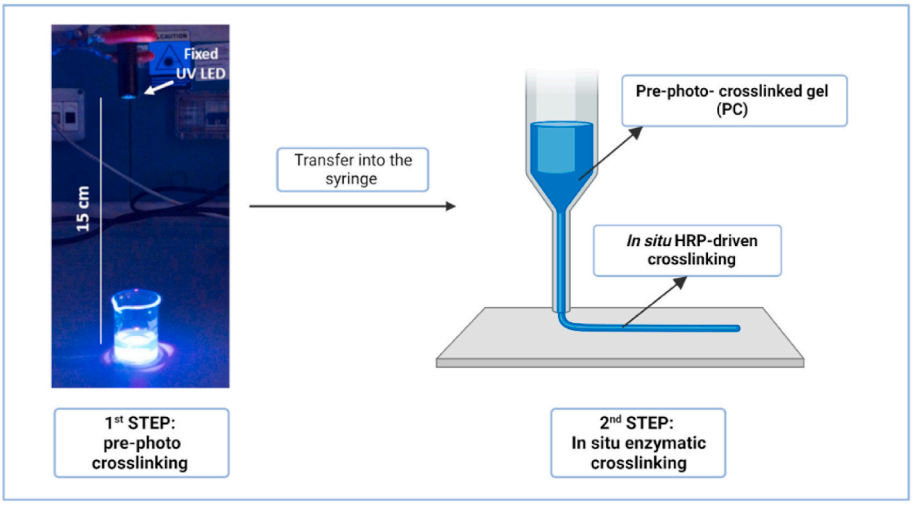

Fig. 1. Design of double crosslinking process. First, Sil-Ma (methacrylate silk fibroin) was pre-photo-crosslinked with 365 nm light. Later, the pre-gel was transferred into the printing syringe for 3D printing. The printing bed temperature was 37 °C and after filament deposition the enzymatic crosslinking led to the stabilization of the structure, improving final gelation. Made with Biorender.

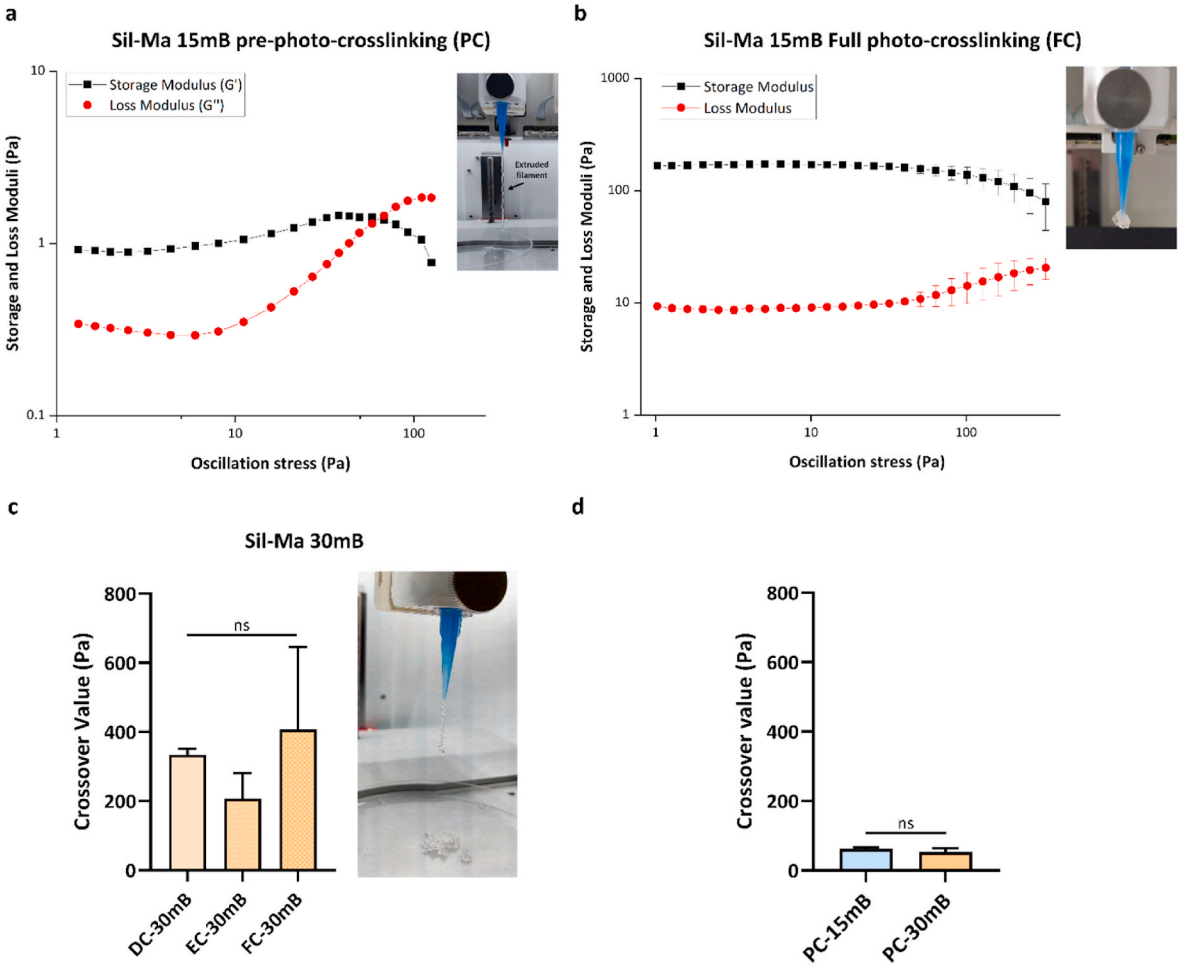

Fig. 2. Viscoelastic analyses to assess ink printability. a) flow point of the pre-photo-crosslinked (PC) condition of 15 mB Sil-Ma and the filament extruded after the pre-gelation. b) full photo-crosslinked (FC) condition of 15 mB Sil-Ma. c) crossover point of the flow points in all the condition studied for 30 mB Sil-Ma. Specifically, DC represents the double crosslinking, EC the enzymatic crosslinking with complete gelation, and the full-photo crosslinked condition (FC). d) flow point of the pre-photo-crosslinked (PC) condition of 15 mB and 30 mB Sil-Ma.

The 30 mB behavior was different compared to the 15 mB (Fig. 2c). All the conditions exhibited a flow point, however, only the PC flow point (Fig. 2d) occurred at relatively low stress (52.6 Pa ±10.5 Pa), with values significantly different compared to the other conditions. These results confirmed the expectation regarding the 30 mB Sil-Ma. First, this was due to the lower molecular weight compared to the 15 mB Sil-Ma and the low concentration used in this work. Indeed, the photo-crosslinking of the methacrylation polymer takes place on primary amine groups, present mainly on lysine residues, which represent a low content in the silk (0.3 %mol) [69] and the lower the MW, the less is the entanglement and length of the chains, thus affecting the kinetics. For this reason, photo-crosslinking efficiency is dependent on silk molecular weight and concentration, resulting in weaker gels compared to the Sil-Ma prepared at higher molecular weight.

However, although in the 30 mB molecular weight, all the conditions exhibited a flow point, the high pressures required to extrude the EC and FC and their variability among the replicates, made the choice of pre-crosslinked conditions clear, repeatable, and resulted in more homogenous filament formation.

After the study of the viscoelasticity properties, rheological tests were performed over time in the LVE region to demonstrate that the pre-crosslinking led to the formation of a pre-gel with low storage modulus. In contrast, the combination of this pre-gel with the HRP crosslinking (double crosslinked condition – DC) led to the formation of a homogenous hydrogel, with significantly higher G' compared to the former condition (Fig. 3). The 15 mB storage modulus increased over time, reaching values around 1594.0 Pa ±44.9 Pa, whereas the 30 mB modulus was 879.0 Pa ±37.2 Pa. It is worth noting that HRP crosslinking has been widely applied to silk fibroin gelation [38,62,66,70–73]. Indeed, among all the parameters, gelation is mainly affected by the molecular weight and concentration of silk. The enzyme has an initial delay phase where gelation is not detectable, and the protein is still liquid. Then, dityrosine bond formation takes place, followed by interchain protein crosslinking. These kinetics proceed over time, leading to further polymerization until the full covalent formation of dityrosine bonds [65]. This is reflected in the increased storage modulus in the double crosslinked condition (DC) up to 72 h. Importantly, the PC condition did not exhibit significant variations over time, and the excessive swelling and weakness of the PC condition after 72 h made it impossible to test at that time point. These results confirmed that the pre-crosslinked was not sufficient to form stable homogenous gels, while proper gel formation was achieved with the double crosslinking.

After rheological analyses, it was clear that fully-crosslinked gels (either enzymatic, photo-cured, and double crosslinked) required high pressure to extrude and that the PC was insufficient to form a stable hydrogel, confirming that the second, enzymatic crosslinking *in situ* was a required fundamental step to further induce the covalent gelation between polymer chains. Therefore, 3D printing was performed by applying the pre-photo-crosslinking, followed by *in situ* activation of the enzymatic crosslinking. Firstly, printability test was performed to measure the accuracy in printing pores inside each structure. As visible in Fig. 4a, although the different infill chosen, the Pr resulted to be very similar between the two conditions. However, it is important to note that not only the Pr was exhibiting values below 1 (1 representing high printing precision), but also that samples exhibited high variability, appreciable from the standard deviations. Moreover, in Fig. 4b some printed structures are shown. For all the printing tests a 22 G and 25 G nozzles was used, demonstrating the suitability and versatility of the pre-crosslinking process for useful extrusion. Smaller diameter nozzles required higher pressures (up to 120 kPa). However, although the Pr discussed before still requires further optimization, the compatibility of the process with printing multilayer structures, or 3D STL models with different resolutions were all feasible.

3.2. Characterization of silk fibroin-based ink

To investigate the stability and behavior of the printed PC and DC conditions, material characterization was performed over 14 days by incubating the samples in medium and water. First, it is worth noting that during the printing of the pre-crosslinked gels (PC), macroscopically different gel consistencies were observed, compared to before printing. For this reason, the investigation of silk secondary structure was performed before and after extrusion, and then monitored at days 1, 7, and 14, for each molecular weight. Fig. 5a shows the infrared spectra for samples before and after extrusion in the range 800–2000 cm^{-1} and Fig. 5b and c show the results of deconvolution of the Amide I (1610-1705 cm^{-1}) band for both MW samples. All the tested conditions, after extrusion, exhibited a shift from silk I to silk II structure, specifically, in antiparallel β-sheets conformation (Fig. 5b, Table S1). Regarding the high molecular weight silk (15 mB), the total amount of anti-parallel β-sheets increased from 21.8% to 41.1% after extrusion, slightly increasing over time (Fig. 5c and d, Table S2). This transition was less evident but present even in the 30 mB Sil-Ma, where the anti-parallel β-sheet content reached 34.8%, increasing at day 1 up to 40–48%

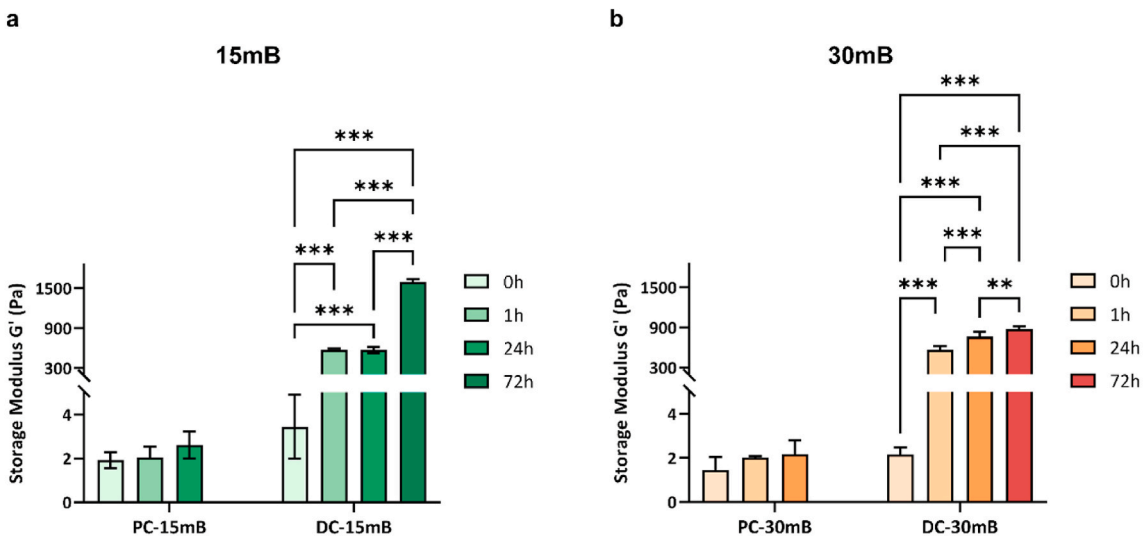

Fig. 3. Storage modulus (G') monitored over time at time point 0, 1, 24, and 72 h for the pre-photo-crosslinked condition (PC) and double crosslinked condition (DC) for both Sil-Ma 15 mB and 30 mB *p < 0.05, **p < 0.01, ***p < 0.001.

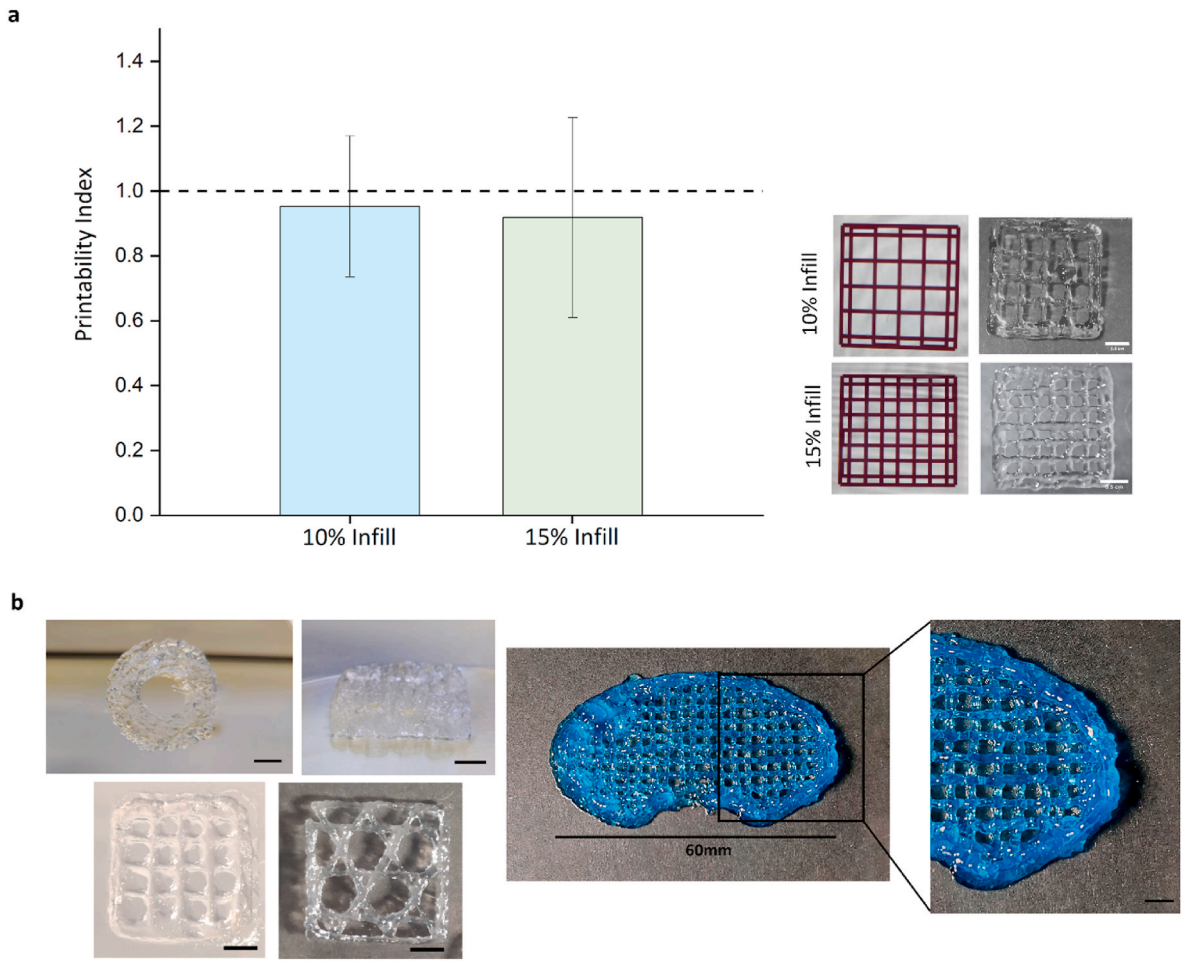

Fig. 4. Printability index measured on DC Sil-Ma printed with 25 G nozzle and two different infill grids, 10% and 15% (a). Printed structures with the double crosslinking process (DC). In blue (dye) some STL 3D models of selected shapes. Scale bar 0.5 cm (b).

(Supplemental Data, Fig. S3, Table S3). The latter effect, the slower transition into crystalline structure for the 30 mB silk compared to the 15 mB, is likely attributed to a lower effect of shear on the protein chains compared to the higher molecular weight. Indeed, it was reported that after shear stimulus, the rearrangements responsible for the amide I shift, might proceed for several hours [74], explaining the slower shift into crystalline structures observed in the 30 mB MW. This conformational transition might be attributed to shear stresses applied inside the nozzle, leading to silk rearrangement toward crystalline (β-sheet) structures, macroscopically responsible of the differences detected in the pre-crosslinked gels after extrusion. Natural silk spinning and artificial extrusion during 3D printing have some similarities [67]. During silk spinning, shear, salt concentration, and pH, play important roles for the fiber formation, thus the solidification of the protein. Specifically, shear might induce silk self-assembly via physical crosslinking [67,75–77]. Our hypothesis is that in aqueous conditions silk in the form of random coils, thus mainly silk I conformation, is surrounded by a water hydration shell created by hydrogen bonding between silk and water. This situation is energetically favorable until the application of the stress in the nozzle which leads to instability of chain conformation, as result of stretching and alignment with consequent breakage of the H-bonds with water [75,76]. This results in a dehydration and the generation of inter- and intra-chain interactions and thus new bonds responsible for the crystalline β-sheet conformation, the thermodynamically stable form of silk structures. Silk fibroin shear-sensitivity, thus aggregation under shear stress, is related to silk fibroin amino acid sequence. Indeed, glycine, alanine, and tyrosine represent 45.9%, 30.3%, and 5.3% of the total amino acidic composition, respectively [78,79]. They are organized into highly ordered, repeated sequences in form of hexamers along the chains. Particularly, the GX repeated sequence where X might be tyrosine, alanine, or serine is mainly responsible for β-sheet structure formation [79–81]. For instance, tyrosine residues, when present in a central position in the repeat sequence close to glycine, are fundamental for creating inter- and intra-chains H-bonding through the –OH group on its aromatic ring, driving structural transitions [79,82,83]. Thus, the silk fibroin sequence composition leads to self-assembly, which under external stimuli as shear can accelerate the transition to silk II conformation. After extrusion, no differences were detected over time in protein secondary structure in Sil-Ma 15 mB, while, as mentioned earlier, the 30 mB rearrangement and stabilization took up to day 1 but then, no significant changes were observed over time. The results for days 1, 7 and 14 for both the PC and DC related to the 30 mB are reported in the Supplemental Data in Fig. S3a and b, as well as the spectra of IR test at day 1 of all the conditions studied (Fig. S3c and d).

In contrast to the initial design, the IR analyses demonstrated that the pre-crosslinked polymer without the addition of the enzymatic crosslinking, exhibited the same protein structure as the double crosslinking – DC, changing its properties when in combination with extrusion stress. Considering the protein rearrangements and dehydration in the nozzle, swelling tests were performed both in medium and water, monitoring water absorbance over time at days 1, 7 and 14. In agreement with the hypothesis, all the conditions for both molecular weights were highly stable over time, with neither significant water absorption nor contraction detected (Fig. 6). Specifically, swelling/contraction

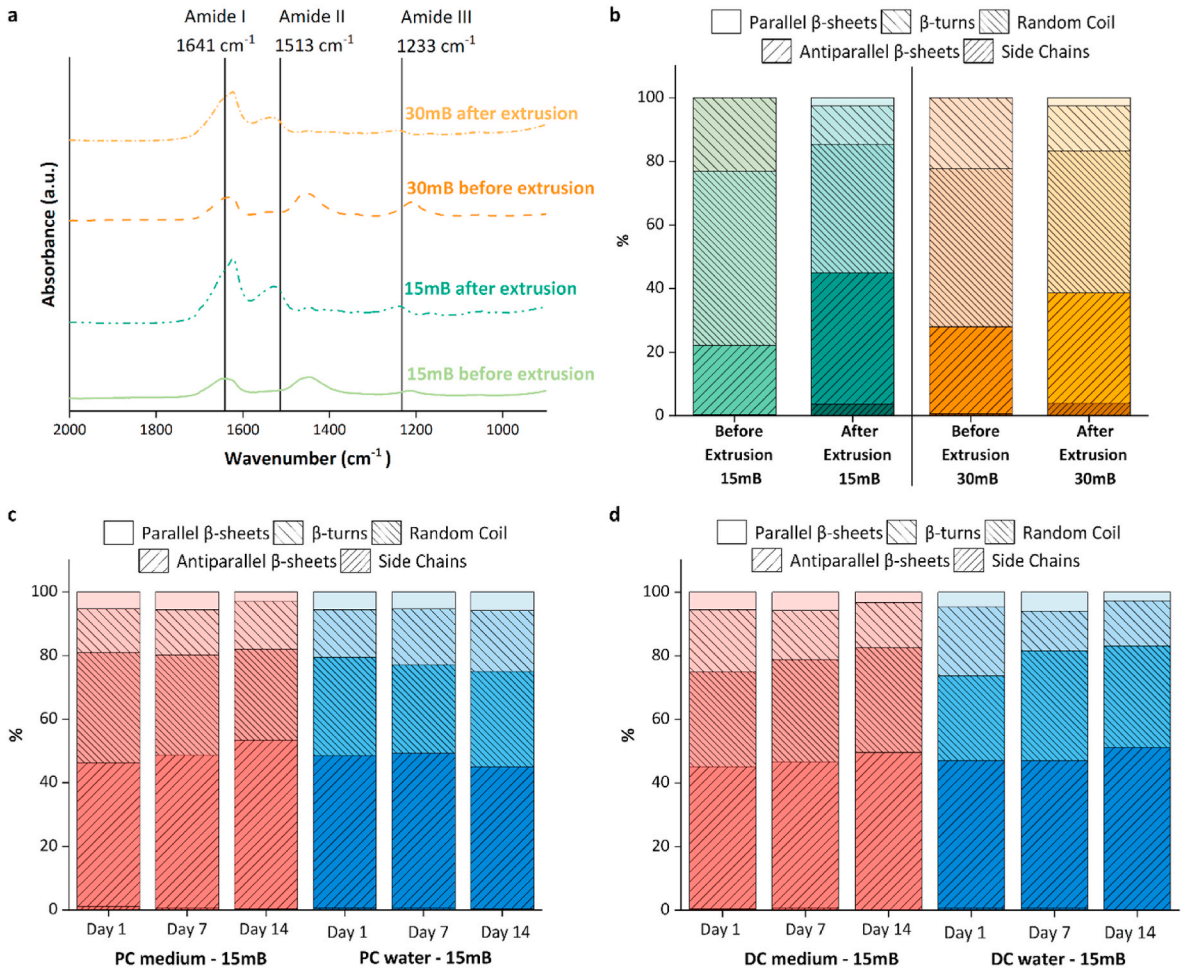

Fig. 5. IR analyses. a) Spectra of both 15 mB and 30 mB Sil-Ma before and after extrusion, both only pre-photo-crosslinked. Silk fibroin amide I, II, and III are visible at 1641, 1513, and 1233 cm^{-} [1], respectively. b) Amide I deconvolution of 15 mB and 30 mB Sil-Ma, before and after extrusion. c) 15 mB Sil-Ma amide I deconvolution of the pre-photo-crosslinked (PC) condition at day 1, 7, and 14 in medium and water; d) Amide I deconvolution of the double crosslinked condition (DC) at day 1, 7, and 14, in medium and water.

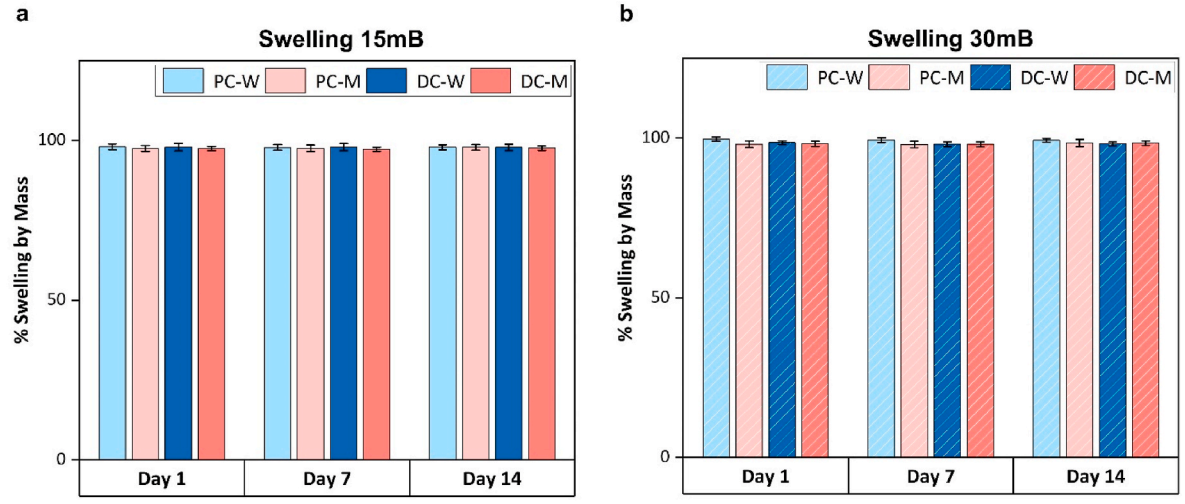

Fig. 6. Swelling tests performed in medium (M) and water (W) on pre-photo-crosslinked (PC) and double crosslinked (DC) gels. Each condition was tested at days 1, 7, and 14. On the left results on Sil-Ma 15 mB, whereas on the right on 30 mB Sil-Ma. No significance differences were detected between the different condition in each time point.

behavior depends on protein concentration, degree of crosslinking, pH, and ionic strength [84,85]. Moreover, during β-sheet formation, water molecules are removed between the β-strands [86]. Therefore, the combination of dehydration and extensive β-crystallization led to the formation of highly stable hydrogels over time.

Taken together these results demonstrated the stability of the materials over the tested conditions. After extrusion, both the pre-crosslinking and the double crosslinking were suitable for *in situ* 3D printing. However, our initial hypothesis was that the pre-crosslinking (PC) condition was unstable compared to the double crosslinking one (DC) since in the latter the HRP-driven gelation led to the formation of stable covalent bonds. For this reason, although the IR and swelling tests did not provide evidence of differences among the conditions, we further characterized the material to verify if our initial hypothesis, the formation of covalent, stable bonds in the double crosslinking condition, was confirmed. The degradation kinetics were assessed both in medium and water, in the presence and absence of enzymes (the latter in the Supplemental Data, in Fig. S4). For degradation studies, protease XIV was selected since it exhibits 390 cleavages sites along the silk fibroin sequence and, compared to chymotrypsin, is able to digest the crystalline structures as well [87]. In Fig. 7, the results after 14 days of digestion are shown. There was a difference between the pre-crosslinked gels (PC) and the double crosslinked (DC), independent of MW. Specifically, in the presence of the enzyme, samples prepared with just the pre-photo-crosslinking process exhibited a significantly faster degradation rate compared to the gels prepared via double-crosslinking (DC).

PC samples at day 14, both the 30 mB and 15 mB conditions, are missing. Indeed, half of these samples were broken and the others difficult to handle without breaking, thus the measurements were not reliable. Furthermore, from degradation tests in the presence of protease, there was a difference in the degradation kinetics between the pre-crosslinked and double crosslinked conditions. The 15 mB condition exhibited similar degradation rates up to day 7 between the PC and the DC, the former rapidly degraded at day 14, whereas the latter was stable with a final residual mass equal to 61% ± 8.15 in water and 61.0% ± 14.74 in medium. For the 30 mB Sil-Ma, some differences were evident at day 1 when the PC in medium degraded significantly more compared to the DC in the same conditions. This difference became clearer at day 7 where PC conditions both in medium and water were significantly more degraded compared to the double crosslinked (DC) conditions. The final residual mass of the DC samples was equal to 65% ± 6.29 in water, and 65.83% ± 3.14 in medium.

Degradation kinetics are dependent on structure-related features, as MW, crystallinity, and secondary arrangements. Generally, silk fibroin degradation is slower compared to other biomaterials, due to the β-sheet features, and protease digests the amorphous regions initially and the crystalline structure last, the latter more resistant to enzymatic cleavage [81,85,87,88]. However, the IR analyses demonstrated that no differences in secondary structure were detected over time among all the conditions, for both molecular weights. In contrast, the degradation tests demonstrated a significant difference between the pre-photo-crosslinking and the double crosslinking processes. Therefore, given the same β-sheet content, the main difference between the pre-crosslinked and double crosslinked conditions should be related to the nature of the bonds in the structures. Specifically, silk fibroin undergoes slower degradation kinetics when chemical and physical crosslinking are combined [88]. Indeed, physical crosslinking leads to the formation of β-sheets through the formation of several hydrogen bonds [80], whereas chemical or enzymatic crosslinking leads to the creation of covalent, permanent, and stable bonds [88,89]. This agrees with our results, since when the HRP is combined with the pre-crosslinking, it induces covalent dityrosine bond formation, synergically working with the already existing physical crosslinking induced by shear stress during extrusion. As result, if the dityrosine bond formation did not affect the overall silk fibroin secondary structure, while at the same time stabilizing these features by forming covalent bonds, thus making the double crosslinked condition (DC) more resistant to the protease cleavage.

Finally, all the conditions were tested in unconfined compression and the Young's modulus calculated over the time points, both in medium and water (Fig. 8). The 15 mB Sil-Ma hydrogels, did not exhibit significant variations over time, whereas the 30 mB at day 14 showed significant differences between the PC and DC, the latter being stiffer compared to the PC. This might be correlated to the presence of weaker bonds in the pre-crosslinked condition, which under compression could easily break and reform in comparison to the covalently bound structures, as in DC. Interestingly, the 15 mB and 30 mB exhibited similar moduli over time, which might be unexpected due to the different molecular weight. However, it is worth noting, that when silk is regenerated, each molecular weight is polydisperse. Specifically, since degumming is a random process, the longer the degumming time, the higher the polydispersity. The 30 mB did not exhibit many differences compared to the 15 mB, whereas they both exhibited differences with much longer degumming times (i.e., 60min) [53]. This explains the

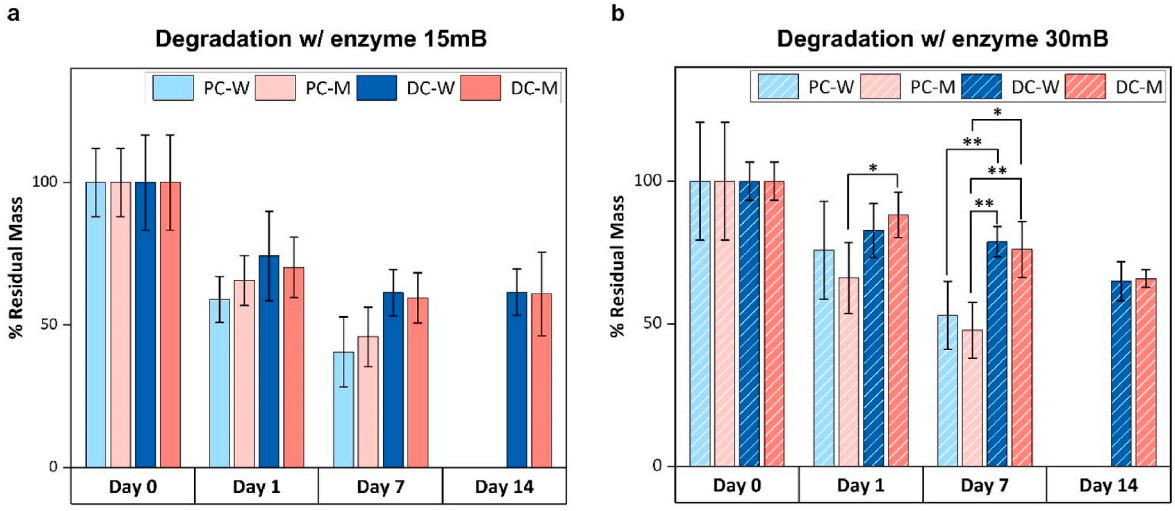

Fig. 7. Degradation kinetics with Protease XIV performed in medium (M) and water (W) on pre-photo-crosslinked (PC) and double crosslinked (DC) gels. Each condition was tested at days 1, 7, and 14. On the left results with Sil-Ma 15 mB (a), on the right with 30 mB Sil-Ma (b). *p < 0.05, **p < 0.01, ***p < 0.001. Where not stated, no significance difference were detected.

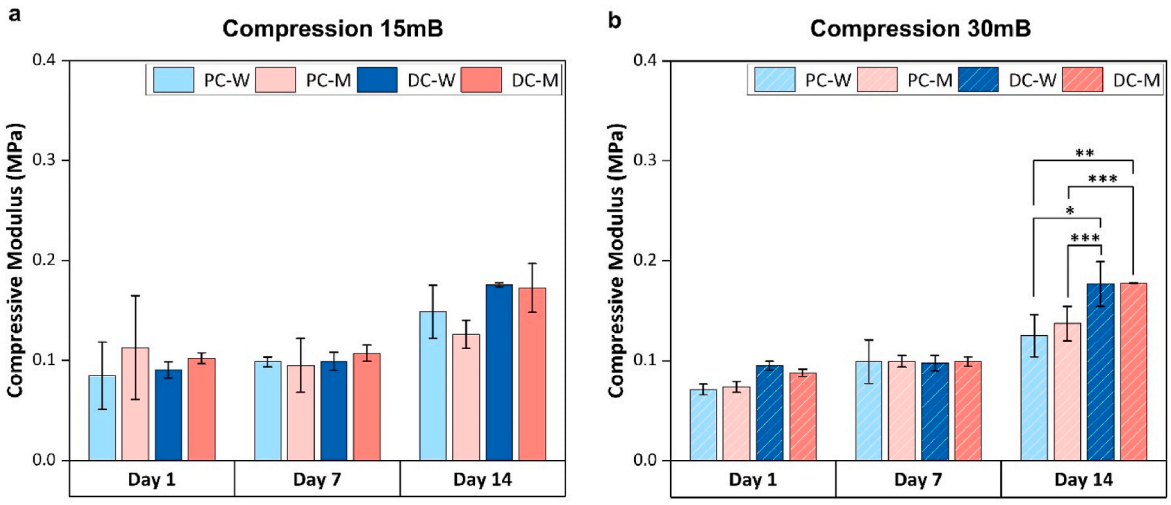

Fig. 8. Young's modulus of the pre-crosslinked (PC) and double crosslinked (DC) conditions, measured at days 1, 7, and 14, after incubation in water and medium, related to the 15 mB Sil-Ma hydrogels (a), and 30 mB Sil-Ma Hydrogels (b). *p < 0.05, **p < 0.01, ***p < 0.001. Where not stated, no significance difference were detected.

absence of differences between the two molecular weights, as they are perhaps too similar in degumming time. This is also visible in the electron microscopy images of DC 15 mB and 30 mB Sil-Ma shown in Fig. S5 in the supplementary materials.

3.3. Preliminary in vitro biological evaluation

After the material characterization, a preliminary biological evaluation was performed to investigate cell viability on the hydrogels, printed as acellular scaffolds. hBM-MSCs were seeded on samples and metabolic activity and cell adhesion were studied by AlamarBlue Assay and confocal imaging, respectively (Fig. 9). All the tested conditions supported cell viability over the 7 days. A significant increase in cell metabolic activity was detected from day 1–7, without any significant differences among the tested conditions and the different molecular weights.

Confocal imaging was performed to evaluate cell adhesion on substrates. In Fig. 9b–l, some representative images of the results obtained are shown. At day 1, cells tended to interact one each other forming clusters (Fig. 9b–d), and some protrusions (Fig. 9b) were observed. After 7 days of culture the cells exhibited an elongated, stretched shape over all the tested conditions (Fig. 9e–l). This different behavior between days 1 and 7 can be explained considering that mulberry silk fibroin (*Bombyx mori*) lacks RGD sequences, important for cell adhesion [90], thus leading to longer times for cells to elongate and spread. However, silk fibroin amino acid composition as well as several factors as topography, porosity, stimuli, and stiffness are crucial in dictating cell behavior on 3D materials [91–93]. Among these, stiffness and gel topography might have positively impacted cell adhesion, leading to the elongation, stretching, and cell-material interactions, as observed at day 7. Additionally, the absence of any differences in terms of cell adhesion and cell shape between the pre-photo-crosslinked (PC) condition and the double crosslinked (DC) suggests that the driving force for cell interactions with the material might be protein rearrangements, not significantly changing among all the conditions and over time, as demonstrated through IR analyses.

The aim of this preliminary experiment was to assess cell viability. However, it is important to mention that only one seeding density was studied, and further studies should explore higher cells density on the scaffolds.

Finally, with a view toward *in vivo* applications, 3D printing of the double crosslinked condition was performed on fresh chicken breast to investigate if the extruded ink adhered to the substrate (Fig. 10). As for all the other tests, the temperature of the printing bed was set at 37 °C. Although this assessment was a preliminary evaluation, the Sil-Ma based ink attached to the chicken breast, without detaching when inverting the substrate (Fig. 10c). Indeed, as reported elsewhere [94,95], silk fibroin exhibits adhesive properties due to its amino acidic composition, such as the serine polar side chains which play a key role in interacting with substrates via the formation of hydrogens bonds. These interactions may also be attributed to the incomplete gelation in the pre-crosslinking phase, leading to a viscous pre-gel which, by completing its gelation *in situ*, allowed the physical interlocking of the gel within the tissue.

Taken together, the results demonstrated that silk fibroin can be tuned to match *in situ* 3D printing requirements by combining two different crosslinking processes including photo- and enzymatic-. Moreover, the characterization of the hydrogels after 3D printing provides useful data for further optimization of the printed shapes to better mimic tissue complexity.

Yet, many challenges must be faced to translate silk-based ink into the clinic for *in situ* applications: the standardization of silk fibroin extraction procedures, the exploration of *in vivo* degradation mechanisms, and the formulation of sterilization processes applicable to the clinical setting, among others. Lastly, the development of silk-based ink with high shelf life and ready to use on demand according to the clinical need is one of the main challenges to work on in future works.

4. Conclusions

Silk fibroin-based inks were designed for *in situ* printing. The versatility of the process was demonstrated on two different molecular weights, and by adapting the fabrication process (i.e., light exposure time), *in situ* 3D printing was achievable. A double crosslinking process was developed, combining pre-gelation via incomplete photo-crosslinking with *in situ* HRP-driven gelation. This led to hydrogels stable over time both in medium and water, with good degradation kinetics over two weeks in the presence of protease type XIV. Additionally, the fundamental role of physical crosslinking induced by extrusion stress in the nozzle led to fast transitions of random coils and β-turn structures toward β-sheets, providing stability in water and medium in the swelling study, but more importantly, dictating the degradation kinetics. Although both the PC and DC were good candidates for *in situ* gel formation, the main difference between them was the synergistic effect of the enzymatic, covalent crosslinking in the latter. If on one side it did not affect silk secondary structure conformation, on the other the covalent bonds induced hydrogels more resistant to degradation in presence of

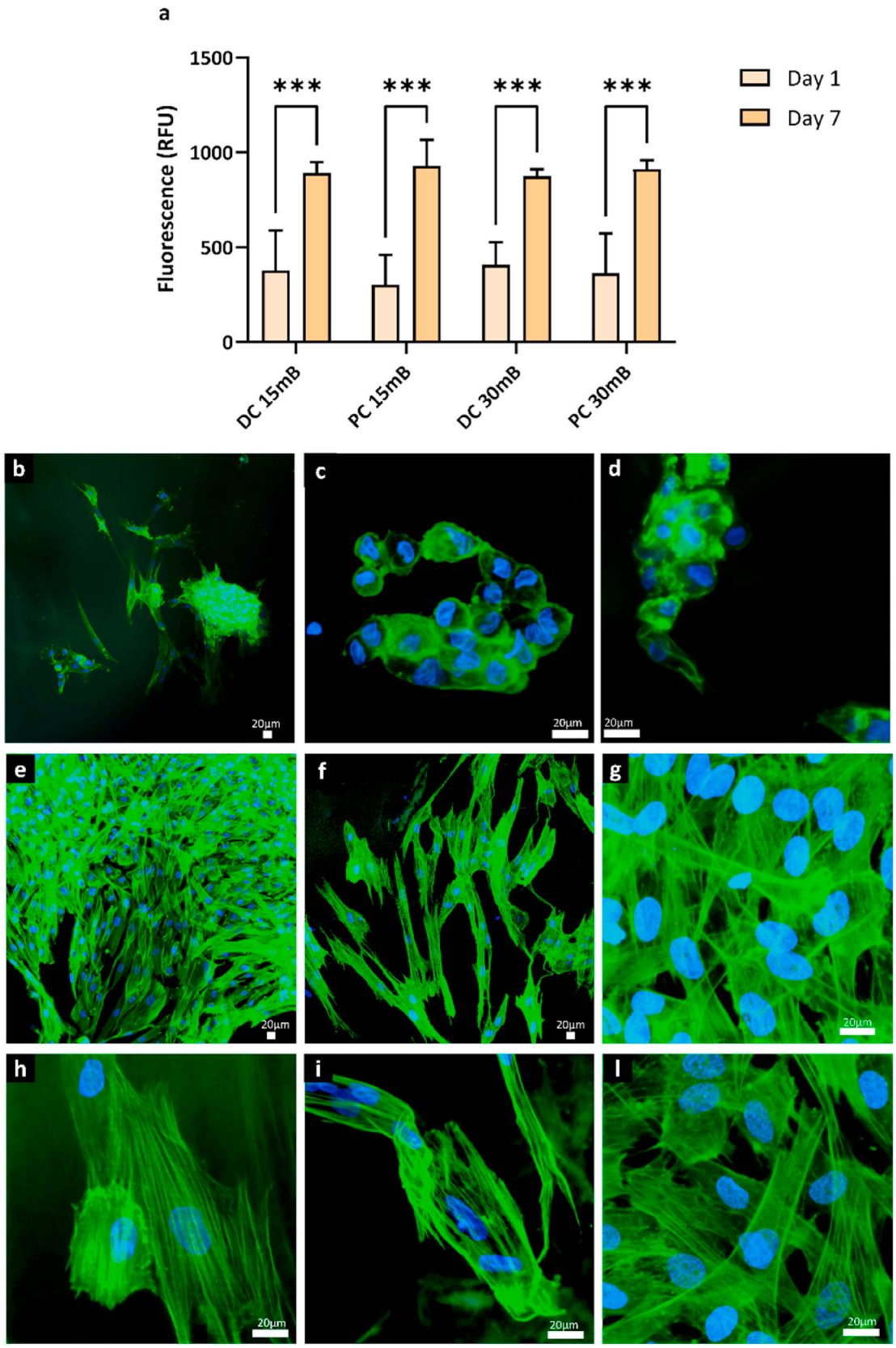

Fig. 9. **(a)** AlamarBlue Assay to monitor metabolic activity over 7 days of culture on Sil-Ma 15 mB double crosslinked (DC 15 mB) and pre-photo-crosslinked (PC 15 mB), Sil-Ma 30 mB double crosslinked (DC 30 mB) and pre-photo-crosslinked (PC 30 mB). ***$p < 0.001$. Confocal images at day 1 **(b–d)** and day 7 **(e–l)**, representative of cell behavior on hydrogels. Different magnifications of hBM-MSCs cytoskeleton (in green) and nuclei (blue) on b) DC 30 mB (double crosslinked), c) DC 15 mB (double crosslinked), d) PC 30 mB (pre-crosslinked). e) DC 30 mB (double crosslinked), f) DC 15 mB (double crosslinked), g) DC 30 mB (double crosslinked), h) DC 15 mB (double crosslinked), i) PC 15 mB (pre-crosslinked), l) PC 30 mB (pre-crosslinked).

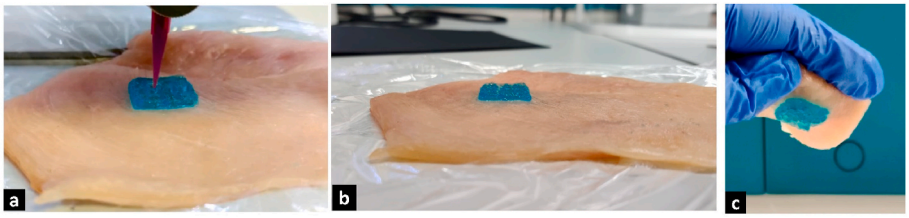

Fig. 10. *In situ* printing on chicken breast of double crosslinked Sil-Ma with 25 G nozzle.

protease, compared to the pre-crosslinked counterpart. This demonstrated that silk fibroin ink properties can be tuned according to the final application.

It is important to note that starting solutions with low concentrations were used. Nevertheless, by combining the covalent crosslinks with the physical ones, hydrogels were obtained with compressive moduli and swelling behavior different from gels prepared without printing [85]. This simplifies the fabrication process, avoiding challenging steps such as silk fibroin concentration, to improve consistency in gel outcomes.

Ethics approval and consent to participate

Nothing to declare.

CRediT authorship contribution statement

Francesca Agostinacchio: Writing – review & editing, Writing – original draft, Visualization, Validation, Methodology, Investigation, Formal analysis, Data curation, Conceptualization. **Vincent Fitzpatrick:** Writing – review & editing, Visualization, Investigation, Conceptualization. **Sandra Dirè:** Writing – review & editing, Visualization, Supervision, Conceptualization. **David L. Kaplan:** Writing – review & editing, Supervision, Resources, Funding acquisition, Conceptualization. **Antonella Motta:** Writing – review & editing, Supervision, Resources, Funding acquisition, Conceptualization.

Declaration of competing interest

None.

Acknowledgements

This project received funding from the Italian Ministry for Education, University, and Research (MIUR) within the program "Departments of Excellence" 2018–2022 (DII-UNITN) and from the European Union's Horizon 2020 research and innovation program under the Marie Sklodowska-Curie grant agreement no. 101008041. We also thank the NIH (P41EB027062) for support of this work.

Appendix A. Supplementary data

Supplementary data to this article can be found online at https://doi.org/10.1016/j.bioactmat.2024.01.015.

References

[1] P. Jain, H. Kathuria, N. Dubey, Biomaterials 287 (2022) 121639.
[2] S. Tripathi, Med. Comm. 4 (2023) e194.
[3] S. Sakai, A. Yoshii, S. Sakurai, K. Horii, O. Nagasuna, Mater. Today Bio 8 (2020) 100078.
[4] S. Raees, F. Ullah, F. Javed, H.M. Akil, M. Jadoon Khan, M. Safdar, I.U. Din, M. A. Alotaibi, A.I. Alharthi, M.A. Bakht, A. Ahmad, A.A. Nassar, Int. J. Biol. Macromol. 232 (2023) 123476.
[5] P.N. Bernal, P. Delrot, D. Loterie, Y. Li, J. Malda, C. Moser, R. Levato, Adv. Mater. 31 (2019) 1904209.
[6] I. Matai, G. Kaur, A. Seyedsalehi, A. McClinton, C.T. Laurencin, Biomaterials 226 (2020) 119536.
[7] N. Hong, G.H. Yang, J.H. Lee, G.H. Kim, J. Biomed. Mater. Res. Part B Appl. Biomater. 106 (2018) 444–459.
[8] Z. Zhu, H.S. Park, M.C. Mcalpine, Sci. Adv. 6 (2020) eaba5575.
[9] F. Agostinacchio, D.L. Kaplan, X. Mu, S. Dirè, A. Motta, Trends Biotechnol. 39 (2020) 719–730.
[10] H. Chen, Y. Zhang, D. Zhou, X. Ma, S. Yang, T. Xu, Biomater. Adv. 142 (2022) 213127.
[11] M. Wang, J. He, Y. Liu, M. Li, D. Li, Z. Jin, Int. J. Bioprinting 1 (2015) 15–26.
[12] C.S. Russell, A. Mostafavi, J.P. Quint, A.C. Panayi, K. Baldino, Z. Bonick, M. Trujillo-miranda, T.J. Williams, J.G. Daubendiek, V. Hugo, S.R. Shin, O. Pourquie, S. Salehi, I. Sinha, A. Tamayol, ACS Appl. Mater. Interfaces 3 (2020) 1568–1579.
[13] A. Macadam, E. Chaudry, C.D. Mctiernan, D. Cortes, E.J. Suuronen, E.I. Alarcon, Front. Bioeng. Biotechnol. 10 (2022) 940896.
[14] C. Di Bella, S. Duchi, C.D. O'Connell, R. Blanchard, C. Augustine, Z. Yue, F. Thompson, C. Richards, S. Beirne, C. Onofrillo, S.H. Bauquier, S.D. Ryan, P. Pivonka, G.G. Wallace, P.F. Choong, J. Tissue Eng. Regen. Med. 12 (2018) 611–621.
[15] C.D. O'Connell, C. Di Bella, F. Thompson, C. Augustine, S. Beirne, R. Cornock, C. J. Richards, J. Chung, S. Gambhir, Z. Yue, J. Bourke, B. Zhang, A. Taylor, A. Quigley, R. Kapsa, P. Choong, G.G. Wallace, Biofabrication 8 (2016), 0.
[16] K. Ma, T. Zhao, L. Yang, P. Wang, J. Jin, H. Teng, D. Xia, L. Zhu, L. Li, Q. Jiang, X. Wang, J. Adv. Res. 23 (2020) 123–132.
[17] M. Samandari, A. Mostafavi, J. Quint, A. Memić, A. Tamayol, Trends Biotechnol. 40 (2022) 1229–1247.
[18] C.D. O'Connell, S. Duchi, C. Onofrillo, L.M. Caballero-Aguilar, A. Trengove, S. E. Doyle, W.J. Zywicki, E. Pirogova, C. Di Bella, Adv. Healthcare Mater. 11 (2022) 1–21.
[19] S. Singh, D. Choudhury, F. Yu, V. Mironov, M.W. Naing, Acta Biomater. 101 (2020) 14–25.
[20] M. Xie, Y. Shi, C. Zhang, M. Ge, J. Zhang, Z. Chen, J. Fu, Z. Xie, Y. He, Nat. Commun. 13 (2022) 3597.
[21] Y. Wu, D.J. Ravnic, I.T. Ozbolat, Trends Biotechnol. 38 (2020) 549–605.
[22] Y. Yang, Z. Yu, X. Lu, J. Dai, C. Zhou, J. Yan, L. Wang, Z. Wang, J. Zang, Bioact. Mater. 26 (2023) 465–477.
[23] A. Fatimi, O. V. Okoro, D. Podstawczyk, J. Siminska-Stanny and A. Shavandi, Gels, DOI:10.3390/gels8030179.
[24] J. Gopinathan, I. Noh, Biomater. Res. 22 (2018) 11.
[25] S. C. Kundu, Silk Biomaterials for Tissue Engineering and Regenerative Medicine, .
[26] J. Choi, J.K. Sahoo, O. Hasturk, T. Falcucci, Y. Yao, D.L. Kaplan, Adv. Mater. Technol. 8 (2023) 2201392.
[27] S. Murchio, M. Benedetti, A. Berto, F. Agostinacchio, G. Zappini, D. Maniglio, Materials (Basel). 15 (2022) 6156.
[28] J.B. Costa, J. Silva-Correia, V.P. Ribeiro, A. da Silva Morais, J.M. Oliveira, R. L. Reis, Mater. Today Commun. 19 (2019) 506–512.
[29] A. Bucciarelli, T. Muthukumar, J.S. Kim, W.K. Kim, A. Quaranta, D. Maniglio, G. Khang, A. Motta, ACS Biomater. Sci. Eng. 5 (2019) 6374–6388.
[30] C.E.G. Miryam Adelfio, Zaira Martin-Moldes, Joshua Erndt-Marino, Lorenzo Tozzi, Margaret J. Duncan, Hatice Hasturk, David L. Kaplan, Adv. Sci. 10 (2023) 2205473.
[31] F. Agostinacchio, D. Maniglio, E. Callone, C. Migliaresi, S. Dire, A. Motta, Soft Matter 17 (2021) 6863–6872.
[32] A. Bucciarelli, A. Motta, Biomater. Adv. 139 (2022) 212982.
[33] J.K. Sahoo, O.H. Jaewon Choi, D.L.K. Marc, L. Descoteaux, Shreyas Mosurkal, Boyang Wang, Biomater. Sci. 8 (2020) 4176–4185.
[34] A.S. Croft, E. Spessot, P. Bhattacharjee, Y. Yang, A. Motta, M. Wöltje, B. Gantenbein, JOR Spine 5 (2022) e1225.
[35] C. Holland, K. Numata, J. Rnjak-Kovacina, F.P. Seib, Adv. Healthcare Mater. 8 (2019) 1800465.
[36] J.K. Sahoo, O. Hasturk, T. Falcucci, D.L. Kaplan, Nat. Rev. Chem. 7 (2023) 302–318.
[37] J. Chakraborty, X. Mu, A. Pramanick, D.L. Kaplan, S. Ghosh, Biomaterials 287 (2022) 121672.
[38] X. Mu, F. Agostinacchio, N. Xiang, Y. Pei, Y. Khan, C. Guo, P. Cebe, A. Motta, D. L. Kaplan, Prog. Polym. Sci. 115 (2021) 101375.
[39] E. Bari, G.M. Di Gravina, F. Scocozza, S. Perteghella, B. Frongia, S. Tengattini, L. Segale, M.L. Torre, M. Conti, Pharmaceutics 15 (2023) 383.
[40] X. Mu, G.-O. Constancio, Z. Xia, J.K. Sahoo, Y.S. Zhang, D.L. Kaplan, Molecules 27 (2022) 2148.
[41] X. Mu, Y. Wang, C. Guo, Y. Li, S. Ling, W. Huang, P. Cebe, H.H. Hsu, F. De Ferrari, X. Jiang, Q. Xu, A. Balduini, F.G. Omenetto, D.L. Kaplan, Macromol. Biosci. 20 (2020) 1–8.

[42] X. Du, D. Wei, L. Huang, M. Zhu, Y. Zhang, Y. Zhu, Mater. Sci. Eng. C 103 (2019) 109731.
[43] J. Yang, C. Deng, M. Shafiq, Z. Li, Q. Zhang, H. Du, S. Li, X. Zhou, C. He, Smart Mater. Med. 3 (2022) 217–229.
[44] K.A.B. Heichel, L. Danielle, Julia A. Tumbic, Marisa E. Boch, Anson W.K. Ma, Biomed. Mater. 15 (2020) 55037.
[45] S.H. Kim, Y.K. Yeon, J.M. Lee, J.R. Chao, Y.J. Lee, Y.B. Seo, M.T. Sultan, O.J. Lee, J. S. Lee, S. Il Yoon, I.S. Hong, G. Khang, S.J. Lee, J.J. Yoo, C.H. Park, Nat. Commun. 9 (2018) 1620.
[46] V. Fitzpatrick, Z. Martín-moldes, A. Deck, R. Torres-sanchez, A. Valat, D. Cairns, C. Li, D.L. Kaplan, Biomaterials 276 (2021) 120995.
[47] J.B. Costa, J. Silva-Correia, J.M. Oliveira, R.L. Reis, Adv. Healthcare Mater. 6 (2017) 1–8.
[48] M.B. Applegate, B.P. Partlow, J. Coburn, B. Marelli, C. Pirie, R. Pineda, D. L. Kaplan, F.G. Omenetto, Adv. Mater. 28 (2016) 2417–2420.
[49] D. Kuang, F. Jiang, F. Wu, K. Kaur, S. Ghosh, S.C. Kundu, S. Lu, Int. J. Biol. Macromol. 134 (2019) 838–845.
[50] X. Cui, B.G. Soliman, C.R. Alcala-Orozco, J. Li, M.A.M. Vis, M. Santos, S.G. Wise, R. Levato, J. Malda, T.B.F. Woodfield, J. Rnjak-Kovacina, K.S. Lim, Adv. Healthcare Mater. 9 (2020) 1–15.
[51] M. Rajput, P. Mondal, P. Yadav, K. Chatterjee, Int. J. Biol. Macromol. 202 (2022) 644–656.
[52] D.N. Rockwood, R.C. Preda, T. Yücel, X. Wang, M.L. Lovett, D. L, Kaplan, Nat. Protoc. 6 (2011) 1612–1631.
[53] B.P. Partlow, A.P. Tabatabai, G.G. Leisk, P. Cebe, D.L. Blair, D.L. Kaplan, Macromol. Biosci. 16 (2016) 666–675.
[54] A. Bucciarelli, M. Petretta, B. Grigolo, L. Gambari, A.M. Bossi, F. Grassi, D. Maniglio, Gels 8 (2022) 833.
[55] A. Maria, B. Devid, Microchim. Acta (2022) 1–9.
[56] S. Park, S.-I. Kim, J.-H. Choi, S.-E. Kim, S.-H. Choe, Y. Son, T.-W. Kang, J.-E. Song, G. Khang, Mol. 28 (2023) 5222.
[57] N. Paxton, W. Smolan, T. Böck, F. Melchels, J. Groll, T. Jungst, Biofabrication 9 (2017) 044107.
[58] F. Perin, E. Spessot, A. Famà, A. Bucciarelli, E. Callone, C. Mota, A. Motta, D. Maniglio, ACS Biomater. Sci. Eng. 9 (2023) 1320–1331.
[59] L. Valot, J. Martinez, A. Mehdi, G. Subra, Chem. Soc. Rev. 48 (2019) 4049–4086.
[60] G. Gao, B.S. Kim, J. Jang, D.W. Cho, ACS Biomater. Sci. Eng. 5 (2019) 1150–1169.
[61] S. Gupta, H. Alrabaiah, M. Christophe, M.R.S. Nadeem, A. Bit, J. Biomed. Mater. Res. (2020) 1–15.
[62] B. Costa, J. Park, A. M. Jorgensen, J. Silva-correia, R. L. Reis, J. M. Oliveira, A. Atala, J. J. Yoo and S. J. Lee, Chem. Mater., DOI:10.1021/acs.chemmater.0c03556.
[63] B.P. Partlow, C.W. Hanna, J. Rnjak-Kovacina, J.E. Moreau, M.B. Applegate, K. A. Burke, B. Marelli, A.N. Mitropoulos, F.G. Omenetto, D.L. Kaplan, Adv. Funct. Mater. 24 (2014) 4615–4624.
[64] R. Aeschbach, R. Amadoò, H. Neukom, BBA - Protein Struct. 439 (1976) 292–301.
[65] A.P. Tabatabai, B.P. Partlow, N.R. Raia, D.L. Kaplan, D.L. Blair, Langmuir 34 (2018) 15383–15387.
[66] B.P. Partlow, M.B. Applegate, F.G. Omenetto, D.L. Kaplan, ACS Biomater. Sci. Eng. 2 (2016) 2108–2121.
[67] X. Mu, V. Fitzpatrick, D.L. Kaplan, Adv. Healthcare Mater. 9 (2020) 1901552.
[68] A. Schwab, R. Levato, M.D. Este, S. Piluso, D. Eglin, J. Malda, Chem. Rev. 120 (2020) 11028–11055.
[69] A.R. Murphy, D.L. Kaplan, J. Mater. Chem. 19 (2009) 6443–6450.
[70] N.R. Raia, B.P. Partlow, M. McGill, E.P. Kimmerling, C.E. Ghezzi, D.L. Kaplan, Biomaterials 131 (2017) 58–67.
[71] Mcgil, L. Meghan, J.M. Grant, D.L. Kaplan, Ann. Biomed. Eng. 48 (2020) 1905–1915.
[72] M. McGill, J.M. Coburn, B.P. Partlow, X. Mu, D.L. Kaplan, Acta Biomater. 63 (2017) 76–84.
[73] O. Hasturk, K.E. Jordan, J. Choi, D.L. Kaplan, Biomaterials 232 (2020) 119720.
[74] M. Boulet-audet, A.E. Terry, F. Vollrath, C. Holland, Acta Biomater. 10 (2014) 776–784.
[75] T. Yucel, P. Cebe, D.L. Kaplan, Biophys. J. 97 (2009) 2044–2050.
[76] Y. Zhang, Y. Zuo, S. Wen, Y. Hu, Y. Min, Biomacromolecules 19 (2018) 1223–1233.
[77] P.R. Laity, C. Holland, Int. J. Mol. Sci. 17 (2016) 1812.
[78] Z. Toprakcioglu, T.P.J. Knowles, Sci. Rep. (2021) 1–10.
[79] M. Mcgill, G.P. Holland, D.L. Kaplan, S. Diego, Macromol. Rapid Commun. 40 (2019) e1800390.
[80] C. Zhou, F. Confalonieri, M. Jacquet, R. Perasso, Z. Li, J. Janin, Proteins struct, Funct. Genet. 122 (2001) 119–122.
[81] C. Guo, C. Li, D.L. Kaplan, Biomacromolecules 21 (2020) 1678–1686.
[82] T. Asakura, K. Suita, T. Kameda, S. Afonin, A.S. Ulrich, Magn. Reson. Chem. 42 (2004) 258–266.
[83] B.P. Partlow, M. Bagheri, J.L. Harden, D.L. Kaplan, Biomacromolecules 17 (2016) 3570–3579.
[84] T.V. Chirila, C. Suzuki, Shuko, papolla, Biotechnol. Appl. Biochem. 64 (2017) 771–781.
[85] J.K. Sahoo, O.H. Jaewon Choi, D.L.K. Marc, L. Descoteaux, Shreyas Mosurkal, Boyang Wang, Biomater. Sci. 8 (2020) 4176–4185.
[86] K. Numata, T. Katashima, T. Sakai, Biomacromolecules 12 (2011) 2137–2144.
[87] D.L. K, Numata Keiji, Peggy Cebe, Biomaterials 31 (2010) 2926.
[88] F. Valente, B.J. Allardyce, M.S. Hepburn, P. Wijesinghe, S.L. Redmond, J. Chen, B. F. Kennedy, R. Rajkhowa, M.D. Atlas, X. Wang, R.J. Dilley, ACS Biomater. Sci. Eng. 6 (2020) 2459–2468.
[89] A.P. Tabatabai, B.P. Partlow, N.R. Raia, D.L. Kaplan, D.L. Blair, Langmuir 34 (2018) 15383–15387.
[90] A. Bandyopadhyay and B. B. Mandal, Biofabrication, DOI:10.1088/1758-5090/ab40fa.
[91] M. Guvendiren, J.A. Burdick, Nat. Commun. 3 (2012) 792.
[92] D. Kochhar, M.K. DeBari, R.D. Abbott, Front. Bioeng. Biotechnol. 9 (2021) 1–11.
[93] P. Rat, B. Marrow, B.B. Mandal, D. Ph, S. Das, D. Ph, K. Choudhury, D. Ph, S. C. Kundu, D. Ph, Tissue Eng. - Part A 16 (2010) 2391–2403.
[94] C.J. Love, B.A. Serban, T. Katashima, K. Numata, M.A. Serban, ACS Biomater. Sci. Eng. 5 (2019) 5960–5967.
[95] E.R. Johnston, Y. Miyagi, J.A. Chuah, K. Numata, M.A. Serban, ACS Biomater. Sci. Eng. 4 (2018) 2815–2824.